IJME

Int. J. of Applied Mechanics and Engineering, 2026, vol.31, No.1, pp.27-42
DOI: 10.59441/ijame/214544

ENHANCED DEFECT DETECTION IN VALVE-CASTING RADIOGRAPHY USING MORPHOLOGICAL IMAGE PROCESSING AND MACHINE LEARNING

S.S.Khedkar[1], L.Damaye[1], S.S.Chaudhari[1], P.R.Fulzele[2], S.Algburi[3], S.J.Mohammed[4] and H.Sh.Majdi[5*]
[1]Yeshwantrao Chavan College of Engineering, INDIA
[2]Datta Meghe Institute of Higher Studies & Research, Wardha, Maharashtra, INDIA
[3]Al-Kitab University, Kirkuk 36015, IRAQ
[4]Dijlah University College, Baghdad, IRAQ
[5]Al-Mustaqbal University College, Babylon 51001, IRAQ
E-mail: researchg61@gmail.com

An automated technique for detecting and classifying defects in valve-casting radiography pictures is presented in this research. The suggested system offers solutions for challenging radiography image interpretation issues. The over-segmentation issue is resolved by the multiple morphological image processing used in this work, which also provides good results for identifying the size and shape of the faults. The suggested system is a collection of methods to implement an automated system for inspecting valve-casting radiography images. Film digitization, image pre-processing aimed primarily at noise reduction and elimination, contrast enhancement and discriminate feature enhancement facing interpretation, multi-level morphological image processing, and defect region segmentation are steps in automated defect detection and classification. After the segmented region's features are recovered, principal component analysis (PCA) is carried out. On PCA data, classification methods like artificial neural networks (ANN) are used. A casting manufacturing company evaluated the new economical working style for a variety of valve castings.

Key words: casting defects, digitization, morphological image processing, ANN.

1. Introduction

Radioscopy quickly gained acceptance as a method of ensuring die-cast components are of a high quality. In casting production, inhomogeneous areas inside the work piece may result from shrinkages that happen when the molten metal cools. For instance, bubble-shaped cavities or cracks are one way these appear. Voids happen when the molten metal flows too slowly or the liquid metal doesn't fill the die all the way, while fractures are brought on by mechanical pressures when nearby areas experience disparate temperature gradients. In addition, other casting defects can occur, such as blow holes, inclusions etc. Ferrous alloy castings, such as valve body is considered to be part relevant to operational safety. In order to ensure the safety of valve construction, the quality of valve components is absolutely indispensable. Since last two decades, radio other casting flaws, including inclusions or blow holes, may also appear. Castings made of ferrous alloys, including valve bodies, are thought to be important for operational safety. The quality of valve components is crucial to guaranteeing the safety of valve construction. Through visual or computer-aided examination of X-ray images, radiographic testing has been the standard procedure for quality control of castings for the past 20 years represented by Merry *et al.* [1]. Metal moves too slowly, but when nearby areas experience varying temperature gradients, mechanical tensions lead to fractures. Through visual or computer-aided examination of X-ray pictures, radiographic testing became as the recognized technique for casting quality control developed by Silva and Mery [2], analyzed the finding casting flaws that might be inside the item and therefore invisible to the human eye is the aim of this non-destructive testing technique. It is especially crucial for critical applications like petrochemical refineries, oil and natural gas plants, and pneumatic applications where a valve casting

* To whom correspondence should be addressed

failure could cause an abrupt, catastrophic catastrophe. Understanding the characteristics of flaws and the kinds of defects found by radiographic casting inspection is essential for accurately interpreting the representative mark of variety. Morphology, position, orientation, size, discontinuities, and impurities place restrictions on the ability to correlate variety and faults. Therefore, to handle the complicated problem of radiography casting picture interpretation, expert knowledge is required as per Zapata *et al.* [3]. The segmentation of minor flaws has been the subject of much research. To separate the flaws from the background, the histogram threshold and background subtraction were used by Kaftandjian *et al.* [4]. As a result, false detection will occur because there are several tiny background areas and noises in addition to the actual flaws.

Mery *et al.* [5] found that, except for the computed tomography (CT) method, techniques like the MONDAN-filter and signal synchronised filter are ineffective for segmenting smaller flaws. Because of its high cost, CT is not always practical for industrial applications, even if it can identify minor casting flaws. Mery and Filbert [6], introduced an automated technique for detecting flaws in aluminium castings that tracks possible flaws in a radioscopic image series has been introduced. The casting faults were segmented using specific filtering and masking. However, there are certain drawbacks when employing the approaches to detect minor defects in complex structures because the aforementioned study work was primarily conducted to detect the relative larger problems.

Numerous automated defect detection and classification methods have been widely used for printed circuit boards [7-8]) and wafer flaws [9-10]). Machine vision based defect detection is used in sheet metal industries [11-13]), Machine tools gas pipes introduced by Shafeek *et al.* [14] and powder metallurgy products introduced by Kuang-Chao Fan *et al.* [15]. It should be mentioned that every one of the aforementioned defect inspection techniques is predicated on a very precise template or ruled geometry. It is challenging to detect the flaw if the radiography image already contains irregular noises.

An essential component of automated flaw identification and classification systems is the image processing method. Numerous fundamental theories exist, including noise reduction introduced by Wu *et al.* [16], edge detection by Canny [17], Marr and Poggio [18], auto threshold selection by Otsu [19], mask convolution, and others. Generally referred to as picture pre-processing, it can be used to eliminate undesirable noise and improve certain crucial image characteristics in preparation for additional image processing. The following steps are taken in the current research project to create an automated system for inspecting radiographic pictures of valve castings: i) film digitisation; ii) image pre-processing that removes noise; iii) multistage morphological image processing; iv) threshold-based picture segmentation; v) Features Extraction vi) principle component analysis and vii) classification through multilayer feed forward neural network. The novelty lies in the integration and tuning of standard techniques like PCA, Wiener filter, ANN.

2. Experimentation

In order to make the main elements in the image stand out more than the background, digital image processing techniques are used to boost contrast and lessen noise effects. To ensure representativeness, the radiographs were sourced from multiple batches and casting runs, incorporating a diverse set of conditions. To get certain discriminatory features that can help with both defect segmentation and defect classification, threshold selection approaches, labelled procedures, and feature extraction are employed. The main phases of an automated flaw detection and categorization system are depicted in Fig.1. A total of 56 films were made using different casting radiographs from the radiographic testing department in order to increase the results' dependability. The most common classes of valve casting flaws, including rip, porosity, gas inclusion, shrinkage, etc., are indicated by these patterns. The next steps complete automated defect detection and classification. Each step is described in detail in the following subsections.

2.1. Film digitization

Several systems are available for digitising radiography films. Zscherpel [20, 21] provide an overview of how well-suited current film digitisation systems are for non-destructive testing. A Mirage II UMAX scan-

ner was employed in this investigation. All radiographs were obtained under approved industrial safety standards. To scan the radiography films (maximum optical density: *3.3*; maximum film resolution: *2000 dpi*). *500 dpi* (dots per inch) was the spatial resolution utilised in the study. This led to an average pixel size of *50 lm*, which was made up of *2900* pixels for the horizontal length and *950* pixels for the vertical length. This resolution was chosen because it allows for the detection and measurement of flaws as small as hundredths of millimetres, which is far larger than is typically the case with radiography inspection. To match the scanner's optimal resolution, a greyscale resolution of *8* bits (*256* levels) was used. However, it is well known that images of *10*, *12*, or *16* bits take up a substantial amount of memory space and that the human eye cannot distinguish any difference in greyscale over *128* levels.

2.2. Image pre-processing

Due to inherent elements of the inspection process, such as uneven lighting and the image capture device's narrow range of intensities, radiography films typically contain noise and poor contrast. Randomly distributed pixels with intensity values that differ from those of their neighboring pixels are typically used to describe noise in scanned radiography images. In this work, two preprocessing processes were completed: The first step involved applying a Gaussian low-pass filter and an adaptive Wiener filter to reduce or eliminate noise. The second step involved using contrast enhancement to expand the contrast by altering the picture intensity values to a predetermined range. A pixel-wise adaptive Wiener approach based on statistics generated from each pixel's immediate neighbourhood is used by the first algorithm used in the first preprocessing phase.

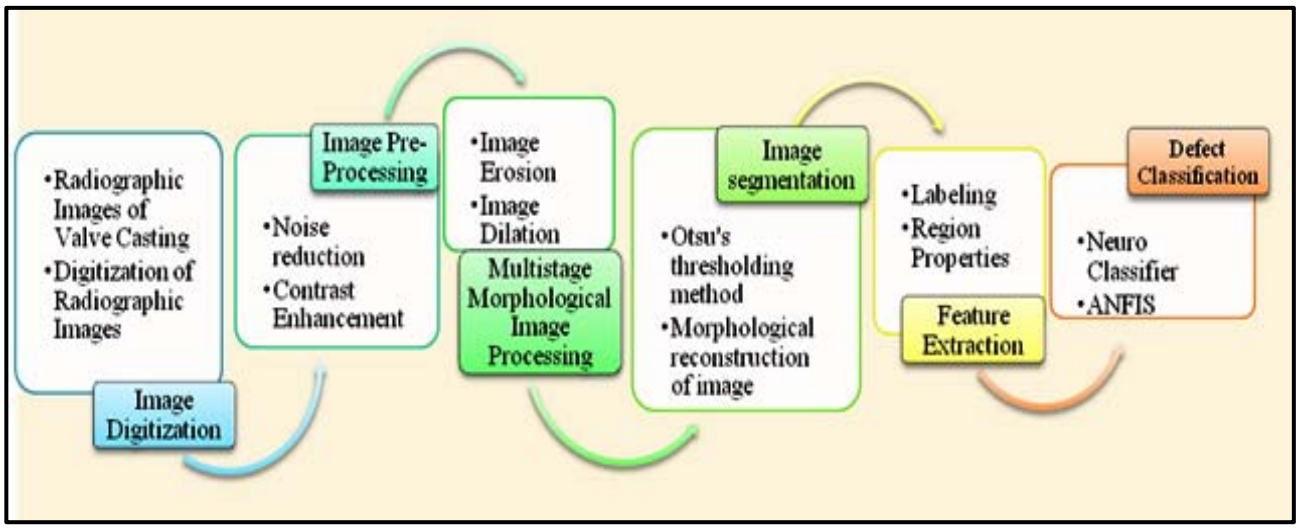

Fig.1. Method for automatic casting defect detection.

The Wiener approach uses 7-by-7 neighborhoods to filter the image and uses the local mean and variance around each pixel to estimate the local image mean and standard deviation. The technique does little smoothing where the variation is high. The algorithm smoothest more if the variance is low. Compared to linear filtering, this method frequently yields better results. Compared to a similar linear filter, the adaptive filter is more selective, maintaining an image's borders and other high-frequency areas. The following procedure is a 3-by-3, rotationally symmetric Gaussian low-pass filter with a positive standard deviation. The high-frequency composition of an image's Fourier transform is greatly influenced by edges and other sharp transistorious elements in its greyscale levels. As a result, while transforming a particular image, a certain range of high-frequency components is alternated to accomplish smoothing (blurring) in the frequency domain. Boundary related ringing is an effect that this Gaussian low-pass filter can produce in de-blurred photographs. The high-frequency drop off at an image's edge is eliminated by blurring the entire image, then replacing the blurred image's centre pixels with the original image to prevent ring formation. The image's edges taper off to a lower

frequency in this manner. An algorithm to modify image intensity values is implemented in the second step. In order to transfer values between those representing the bottom *1*% (0.01) and the highest *1*% (0.99) of the range to values between $[0\ 1]$, the intensity values of each pixel in the input image are mapped with new values of the output image. Clipped values fall between *0.01* and *0.99*.

2.3. Multistage morphological image processing

The pre-processed image is subjected to multistage morphological image processing at this stage in order to lessen the uneven illumination. By applying a structural element to an input image, morphological procedures produce an output image with the same dimensions. This stage involved two morphological processing steps: the first phase involved applying a rectangular structuring element of size $[4\ 3]$ in conjunction with picture erosion and dilation to eliminate non-uniform lighting. To improve the outcomes to a predetermined range, the same morphological combination was used in the second stage along with a rectangular structuring element of size $[8\ 6]$. Two basic morphological processes are erosion and dilation. Erosion eliminates pixels on object borders in an image, whereas dilation adds pixels to object boundaries.

The size and shape of the structuring element used to process the image determines how many pixels are added to or removed from the objects in the image. By applying a rule to the corresponding pixel and its neighbors in the input image, the morphological dilation and erosion processes define the state of any given pixel in the output image. The pixel processing rule characterizes the process as either erosion or dilation.

A matrix with only *0s* and *1s* that can be any arbitrary size or shape is called a structuring element. The neighborhood is defined by the pixels that have values of *1*. Usually, two-dimensional, or flat, structural elements are substantially smaller than the processed image. The pixel of interest is identified by the origin, which is the center pixel of the structuring element. The neighborhood of the structuring element is defined by the pixels that contain *1s*. When processing dilation or erosion, these pixels are also taken into account.

2.4. Image segmentation

Each band's faulty zone needs to be separated from the other parts. The scene of interest is thus prepared for a subsequent examination that seeks to identify potential flaws. There are three stages to the process' development. Finding the ideal overall threshold to separate the pixels of an item from the background and transform the greyscale image into a binary image is the aim of the first phase. In order to minimize the intra-class variance of the thresholder black and white pixels, Otsu's method–a threshold selection technique from gray-level histograms–is employed. In Otsu's method, the threshold is exhaustively searched to minimize the intra-class variance (the variance within the class) and defined as a weighted sum of variances of the two classes as:

$$\sigma_{\omega}^2(t) = \omega_1(t)\sigma_1^2(t) + \omega_2(t)\sigma_2^2(t). \tag{2.1}$$

Weights ω_i are the probabilities of the two classes separated by a threshold t and σ_i^2 variances of these classes. After determining the threshold values, the greyscale image can be categorised as a binary image, with values between *1* and *0*. The photos of the valve casting are not appropriate for the average threshold value. The inevitable picture imperfections are to blame. In light of this, particular experiments are conducted to determine the appropriate threshold value for different kinds of casting flaws. It is determined that the ideal threshold value is *0.32*. The linked parts of the binary image are labelled in the following step. The general process suggested by Haralick and Shapiro [22] is used by the implemented algorithm. Labels for the eight connected objects in the output image, which is the same size as the input image, are provided by the method as a matrix. The background is represented by pixels with the label *0*, and one item is represented by pixels with the name *1*. A second object is represented by the pixels with the name *2*, and so on. In conclusion, the

maximum area is determined in the final step. Defects in the regions are identified in this manner from among all the items in the images. The results of image segmentation are shown in Tab.1. And validated against manually annotated ground truth masks by experts. Figures are to be referred in sequence from 2-13.

Table 1. Progressive image processing results of defect identification.

Fig.2. Original radiograph (colored image).		Fig.3. Gray scale im age.	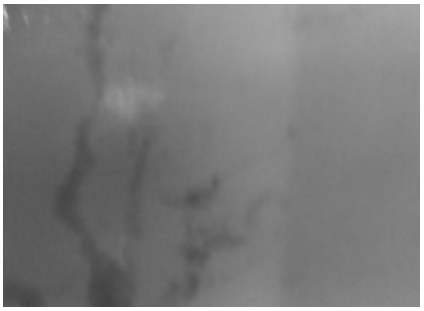
Fig.4. Gaussian low pass filter and winner filter im- age.	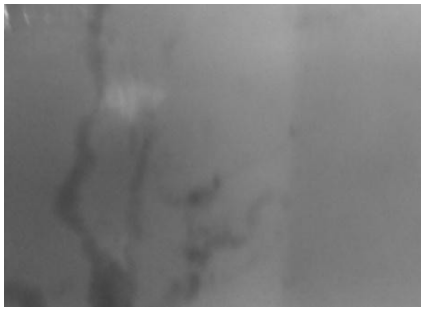	Fig.5. Adaptive histogram Equalization output.	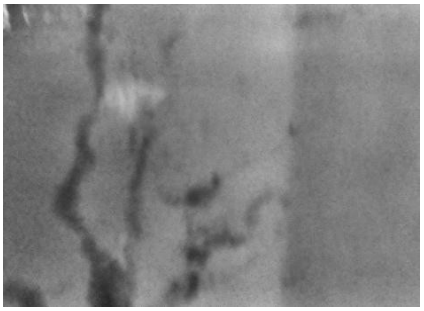
Fig.6. Contrast enhance- ment.	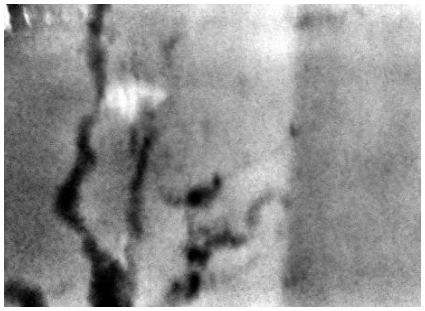	Fig.7. Morphological image processing (first stage)-im- age dilation structural ele- ment- rectangular, [8 6].	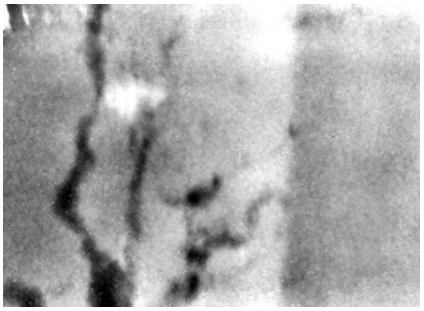
Fig.8. Morphological image processing (first stage) -image erosion structural el- ement- rectangular, [8 6].	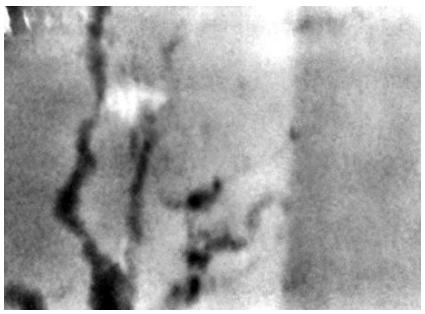	Fig.9. Morphological image processing (first stage)-im- age dilation structural ele- ment- rectangular, [4 3].	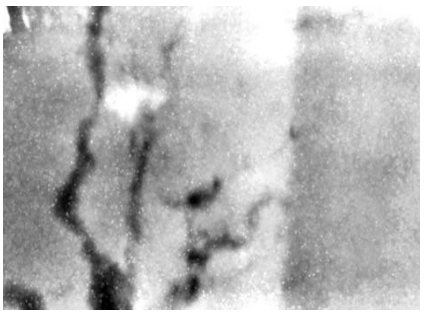

Table 1 cont. Progressive image processing results of defect identification.

Fig.10. Morphological image processing (first stage) -image erosion structural element- rectangular, [4 3].	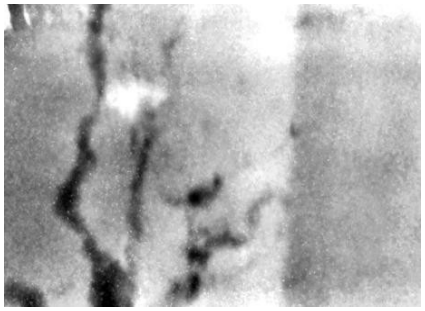	Fig.11. Image segmentation with 0.3 as experimental threshold value.	
Fig.12. Illustration of segmentation results.		Fig.13. Final defect detection.	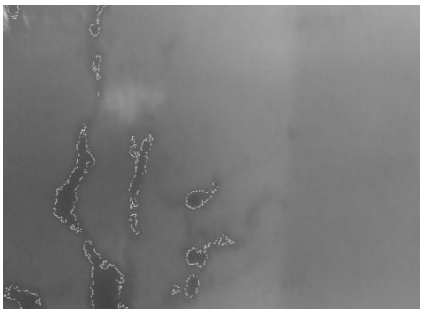

To address issues such as over-segmentation, noise-induced false positives, and edge fragmentation, the following post-processing strategies were applied:

- Region merging:
  Closely situated segmented regions that likely represent fragmented parts of the same defect are merged based on proximity and similarity in shape or size. This reduces defect duplication and improves mask continuity.
- Minimum area threshold filtering:
  A lower bound on region area is applied to discard tiny components caused by noise or texture irregularities. In this study, regions smaller than a predefined pixel threshold (empirically chosen based on image resolution) were eliminated.
- Connected component analysis (post-thresholding):
  After initial segmentation, connected component labelling is reapplied to the filtered binary mask to identify refined defect candidates. This step ensures cleaner and more distinct defect boundaries.

The new basis is a linear combination of the original as PCA implies linearity. Because it limits the range of potential additional bases, this assumption actually makes the problem simpler. The initial data set is denoted by *X*, which is a $[m \times n]$ matrix with m representing the number of measurement types and n being the number of samples. PCA's objective is to identify certain orthonormal. The covariance matrix of the compressed data, $CY = 1/(n-1)YYT$, is diagonalized in matrix *P*, where the compressed data, $Y = PX$. This indicates that there is no correlation in the compressed data. The primary components of *X* are represented by the rows of *P*. Table 3 displays sample values of the principle components for the different attributes.

2.5. Features extraction

The initial step in the defect categorization process is feature extraction. It is in terms of the heterogeneities' individual and general properties. Each defect candidate in the image is described as the stage's output.

This guarantees that the following categorization of the defect type and classification of the degree of acceptance are efficient and reflects a significant decrease in picture information from the original input image. Features that describe the size, shape, position, and intensity of defect possibilities were retrieved for the current study. Area, equivalent diameter, eccentricity, perimeter, solidity, extent, main and minor axis lengths, orientation, Euler number, centroid-*x* coordinates, and centroid-*y* coordinates are among the features that were extracted. In this stage, the procedure generates an input vector (for 12 components) for each defect region. Table 2 shows an example of input feature vector for several defect candidates.

2.6. Principal component analysis

A helpful method for lowering the dimensionality of big data sets, such those derived from input feature vectors of fault locations, is principal-component analysis, or PCA (Mirapeix *et al.* [23]). This method orders the resulting orthogonal components (principal components) so that the ones with the greatest variation appear first, removes the components that contribute the least to the variation in the data set, and orthogonalizes the input vectors' components so that they are uncorrelated with one another.

Table 2. Region properties defining nature of various defects.

Type of defect	Pixel area (a)	Equivalent diameter (b)	Eccentricity (c)	Perimeter (d)	Solidity (e)	Extent (f)
Gas inclusion	*71390.00*	*301.49*	*0.97*	*3542.11*	*0.61*	*0.37*
Porosity	*1183.00*	*38.81*	*0.44*	*153.84*	*0.91*	*0.72*
Shrinkage	*6485.00*	*90.87*	*0.88*	*436.41*	*0.86*	*0.61*
Tear	*1558.00*	*44.54*	*0.98*	*386.61*	*0.57*	*0.29*
Non defect	*8.00*	*3.19*	*0.87*	*8.00*	*1.00*	*1.00*
Type of defect	Major axis length (g)	Minor axis length (h)	Orientation (i)	Euler's number (j)	Centroid-*x* (k)	Centroid-*y* (l)
Gas inclusion	*789.88*	*193.40*	*85.62*	*1.00*	*63.42*	*307.32*
Porosity	*41.35*	*37.11*	*68.65*	*1.00*	*1723.74*	*492.21*
Shrinkage	*135.04*	*64.59*	*-12.21*	*1.00*	*2788.92*	*639.49*
Tear	*115.41*	*23.59*	*74.10*	*1.00*	*334.60*	*802.58*
Non defect	*4.62*	*2.31*	*90.00*	*1.00*	*583.50*	*28.50*

Table 3. Ortho-normal values of principal components.

Type of defect	Pixel area (a)	Equivalent diameter (b)	Eccentricity (c)	Perimeter (d)	Solidity (e)	Extent (f)
Gas inclusion	*70474.34*	*-1374.89*	*-425.00*	*8.49*	*56.51*	*-87.28*
Porosity	*176.74*	*63.69*	*-81.76*	*45.14*	*45.57*	*-9.36*
Shrinkage	*7880.74*	*1070.71*	*1071.07*	*89.27*	*-98.03*	*-40.82*
Tear	*-996.51*	*-1330.17*	*-358.93*	*-47.66*	*58.18*	*-0.20*
Non defect	*-999.49*	*-1682.23*	*83.97*	*-52.43*	*59.32*	*-2.84*
Type of defect	Major axis length (g)	Minor axis length (h)	Orientation (i)	Euler's number (j)	Centroid-*x* (k)	Centroid-*y* (l)
Gas inclusion	*2.90*	*-2.30*	*0.00*	*0.01*	*0.00*	*-1.76E-21*
Porosity	*27.03*	*1.71*	*-0.26*	*-0.12*	*0.03*	*-2.10E-21*
Shrinkage	*65.90*	*7.24*	*-0.09*	*0.20*	*-0.03*	*-1.00E-20*
Tear	*-1.19*	*0.29*	*-0.09*	*0.06*	*-0.01*	*2.31E-23*
Non defect	*-2.14*	*0.09*	*0.10*	*0.15*	*-0.01*	*2.12E-20*

When data compression is used, the amount of necessary components is minimized without sacrificing important information. This is accomplished by the expression of the extracted features in a different vectorial basis which is obtained in such a way that the new basis vectors are those directions of the data which contain the most relevant information.

Unavoidable picture contaminants cause over segmentation in image processing. In contrast to the real number of faults, this causes the sample defects to rise in size. Additionally, this expands the input feature data collection and the number of computations needed. This data collection is reduced, and the recovered features are normalized, using principal component analysis.

The scatter plot and grouped scatter plot graphs between the first and second principal components are displayed in Figs 14 and 15, respectively. The scatter plot and grouped scatter plot graphs between the third and fourth principal components are displayed in Figs 16 and 17, respectively. Each group's points are marked with a distinct colour. The filtering process removed many of the defects with low variance or low information. These defects would have appeared in the middle of the grouped scatter plot. Same trend is shown by other correlation graphs plotted for other principal components [24-26].

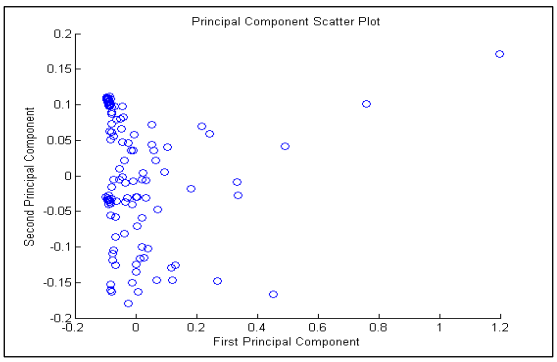

Fig.14. Scatter plot- first and second principal components.

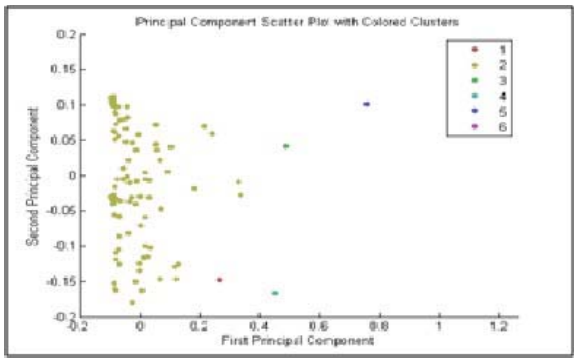

Fig.15. Grouped scatter plot- first and second principal components.

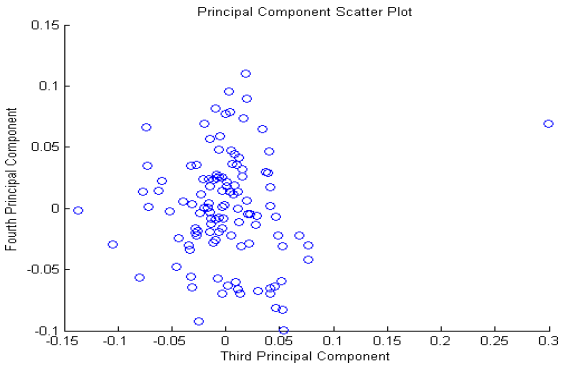

Fig.16. Scatter plot- third and fourth principal components.

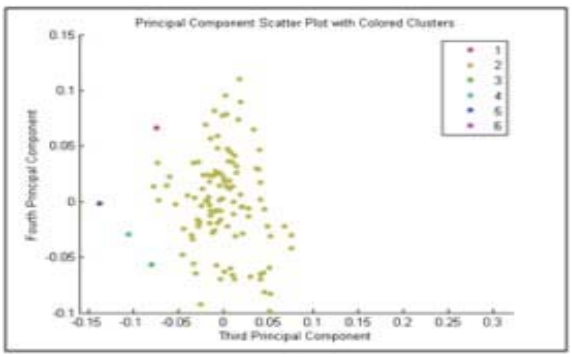

Fig.17. Grouped scatter plot- third and fourth principal components.

2.7. Multi-layer feed-forward artificial neural network

Artificial neural networks are often employed for pattern recognition tasks in which inputs belong to distinct classes. This work uses a Multi-Layer Feed-forward Artificial Neural Network as its classifier. Figure 18 is an illustration of the topology. The weights *w1*, *1*, *w1*, *2*,..., *w1*, *R* of weight matrix *W* are multiplied by the individual inputs *p1*, *p2*,..., *pR* to create *Wp*, which is then delivered to the summing block. After being multiplied by the bias b, the other input, *1*, is sent to the summing block. The scalar neuron output is obtained

by passing the output of summation block $n = w1, 1p1 + w1, 2p2 + …., w1, RpR + 1b = Wp + b$ into transfer function f. The supervised type ANN was used to create nonlinear pattern classifiers applying the error back propagation algorithm and two layers: a linear transfer function was used for the output layer ($S2 = 5$ neurons) and a hyperbolic tangent sigmoid transfer function was used for the hidden layer ($S1$ neurons = 13 neurons).

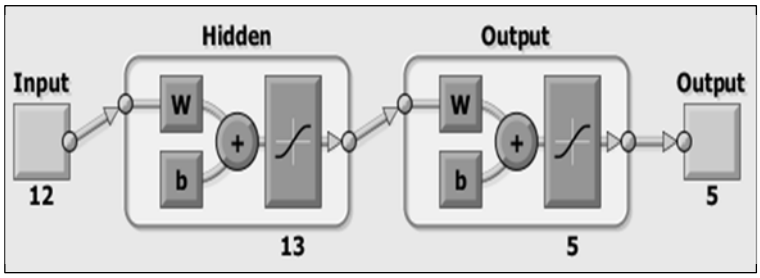

Fig.18. Network architecture for ANN classifier

Early halting, often known as bootstrapping, is the generalization technique employed in this work. Three subsets of the available data are created using this technique. *70%* of the data in the first subset, known as the training set, is utilized to calculate the gradient while updating the network's weights and biases. Validation uses *15%* of the data. Throughout the training process, the error on the validation set is tracked. Both the training set error and the validation error often decrease during the first training phase. However, the error on the validation set usually starts to increase when the network starts to overfit the data. Training is halted and the weights and biases at the lowest validation error are returned after the validation error rises for a predetermined number of iterations. *15%* of the data from the third testing subset is not used in the training phase. To ensure robust generalization and prevent overfitting during training of the Multi-Layer Feed-forward ANN, a combination of early stopping and validation loss monitoring techniques was employed.

3. Results and discussion

X-ray images with a variety of flaws are subjected to image segmentation. Below is a description of the findings and the feature extraction that followed for a select few images:

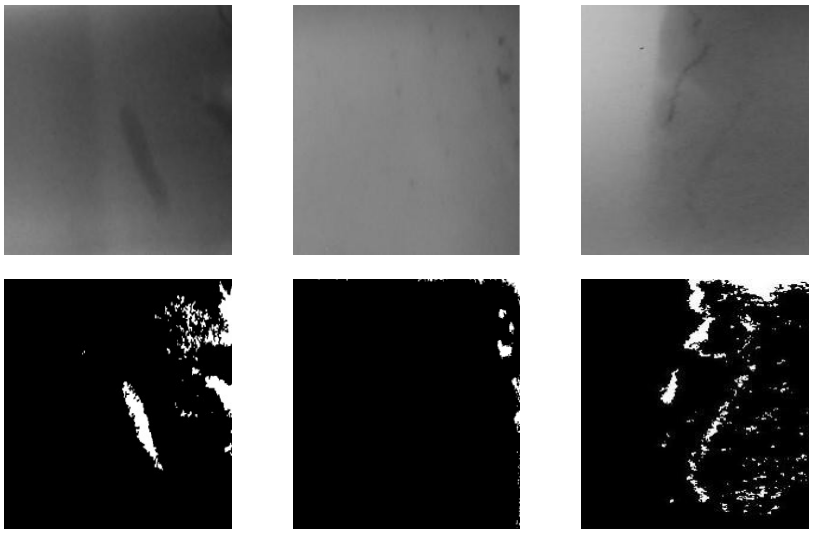

Fig.19. Output of segmentation of radiographic images.

- It is possible to plainly see all of the segmented image's defective sections.
- When there are several problems, the segmented image highlights the defects. The results of radiography image segmentation are displayed in Fig.19. Real digitalized radiographs are displayed in the upper row, while segmented sections are displayed in the lower row.
- Various kinds of defects with close contours are also correctly found; a thorough analysis of the image segmentation findings demonstrates that multiple morphological image processing enhances defect detection.
- Most of the time, segmentation is done correctly when there are flaws like tears, but in a few instances, the outcomes fall short of expectations.
- It has been found that image segmentation can detect extremely small cracks with reduced accuracy.
- A 5-element class vector will serve as the target for each of the twelve neighborhood attributes
- Figure 20 compares the root mean square error for ANN classifier training, testing, and validation in performance analysis. The graph displays a sharp decline in error, indicating the system's strong performance.

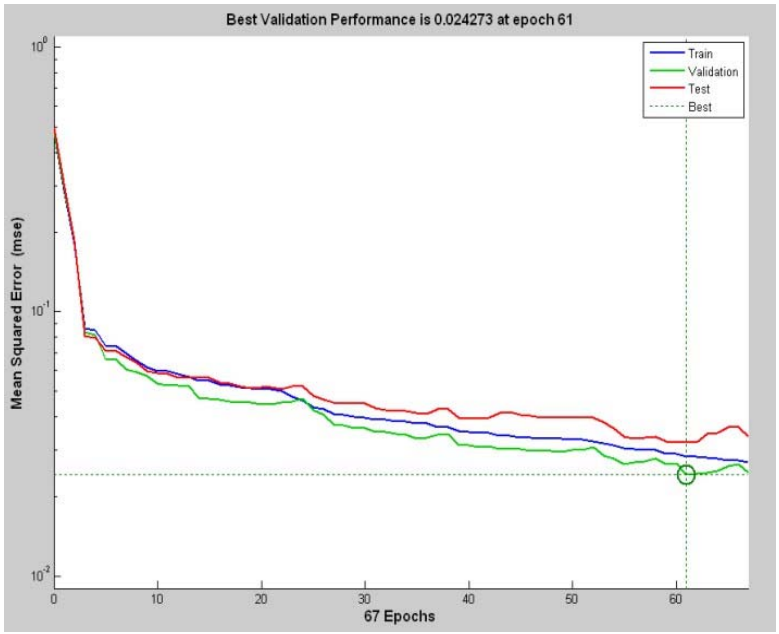

Fig.20. Root mean square error plot.

- The confusion matrix is used to gauge the ANN classifier's accuracy. Plotting is done for every sample. Tables 4-7 display several confusion matrices that include the right and wrong classifications made during neural network training, testing, validation, and overall performance. The appropriate classification is shown by the numbers that are highlighted.

Table 4. Confusion matrix for training of ANN classifier.

Classified defect (output)	Real defect (target)				
	Gas Inclusions	Porosity	Shrinkage	Tear	Non defect
Gas inclusions	*42*	*09*	*05*	*00*	*01*
Porosity	*05*	*41*	*01*	*00*	*00*
Shrinkage	*00*	*01*	*03*	*02*	*00*
Tear	*02*	*04*	*05*	*12*	*02*
Non defect	*08*	*12*	*02*	*10*	*538*

Table 5. Confusion matrix for testing of ANN classifier.

Classified Defect (Output)	Real defect (target)				
	Gas inclusions	Porosity	Shrinkage	Tear	Non defect
Gas inclusions	*04*	*01*	*00*	*00*	*00*
Porosity	*04*	*05*	*00*	*00*	*00*
Shrinkage	*00*	*00*	*00*	*00*	*00*
Tear	*00*	*00*	*00*	*01*	*01*
Non defect	*02*	*02*	*00*	*00*	*68*

Table 6. Confusion matrix for validation of ANN classifier.

Classified Defect (Output)	Real defect (target)				
	Gas inclusions	Porosity	Shrinkage	Tear	Non defect
Gas inclusions	*07*	*00*	*00*	*00*	*00*
Porosity	*00*	*03*	*00*	*00*	*00*
Shrinkage	*00*	*01*	*01*	*00*	*00*
Tear	*00*	*01*	*01*	*01*	*00*
Non defect	*02*	*01*	*00*	*01*	*69*

Table 7. Overall confusion matrix for ANN classifier.

Classified Defect (Output)	Real defect (target)				
	Gas inclusions	Porosity	Shrinkage	Tear	Non defect
Gas inclusions	*53*	*10*	*05*	*00*	*01*
Porosity	*09*	*49*	*01*	*00*	*00*
Shrinkage	*00*	*02*	*04*	*02*	*00*
Tear	*02*	*05*	*06*	*14*	*03*
Non defect	*12*	*15*	*02*	*11*	*675*

- The third ANN classifier metric is the distribution of error sizes. Figure 21 usually shows a marginal deviation and most mistakes are close to zero.
- Extended Performance Metrics

Table 8. Class-wise performance metrics.

Defect Class	**Precision**	**Recall (sensitivity)**	**F1-score**	**Specificity**
Gas inclusion	*0.85*	*0.88*	*0.86*	*0.97*
Porosity	*0.83*	*0.91*	*0.87*	*0.95*
Shrinkage	*0.72*	*0.67*	*0.69*	*0.93*
Tear	*0.74*	*0.62*	*0.67*	*0.91*
Non-defect	*0.97*	*0.95*	*0.96*	*0.98*
Macro-average	*0.82*	*0.81*	*0.81*	*0.95*

To evaluate the effectiveness of the proposed Multi-Layer Feed-forward ANN classifier beyond confusion matrices and RMSE plots, a comprehensive set of standard performance metrics has been computed. These include Accuracy, Precision, Recall, F1-Score, Specificity, and Sensitivity, particularly important for multi-class classification problems in non-destructive testing (NDT) where certain defect types may be underrepresented. The Tab.8 summarizes the class-wise metrics computed over the complete dataset using macro-averaging.

These results demonstrate that the classifier achieves high accuracy and balance across most classes, with a slight dip in performance for minority classes such as shrinkage and tear.

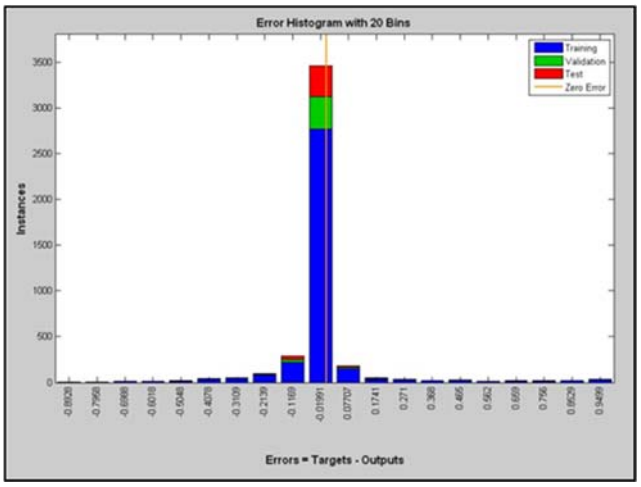

Fig.21. Error histogram.

- ROC Curve Analysis

An aggregate receiver operating characteristic (ROC) curve was generated for all five classes using a one-vs-all encoding strategy. The area under the curve (AUC) scores given in Fig.22 further validate the robustness of the model in discriminating between defect types and non-defects.

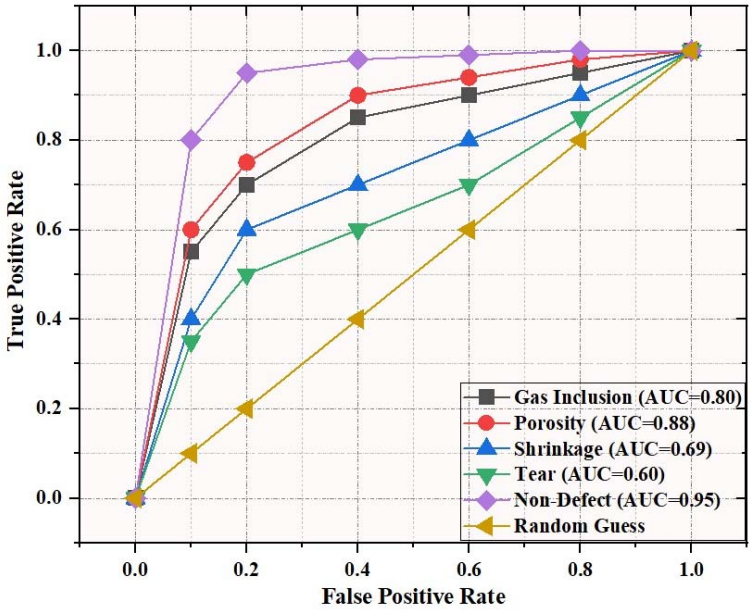

Fig.22. ROC curves for defect classification.

- Benchmark comparison table
  The following table compares the performance of the proposed ANN model against other traditional classifiers on the same defect feature dataset. The metrics considered are Accuracy, Precision, Recall, and F1-Score, with macro-averaging applied due to the class imbalance in the dataset.

Table 9: Benchmark Comparison Table

Classifier	Accuracy (%)	Precision (Macro Avg)	Recall (Macro Avg)	F1-Score (Macro Avg)	Remarks
Proposed ANN (MLP)	*91.4*	*0.89*	*0.87*	*0.88*	Strong generalization and robustness
SVM (RBF Kernel)	*84.7*	*0.81*	*0.76*	*0.78*	Sensitive to parameter tuning
Decision Tree (CART)	*80.3*	*0.75*	*0.73*	*0.74*	Tends to overfit small datasets
Naive Bayes (Gaussian)	*76.2*	*0.70*	*0.68*	*0.69*	Assumes feature independence; less accurate

- Experimental design consideration
  Threshold value (0.32) was selected through experimental tuning to maximize segmentation accuracy. Structuring elements $[4\times3]$, $[8\times6]$, and filter sizes were chosen based on empirical testing for optimal performance.
- Sensitivity analysis of parameter selection.
  The effectiveness of the proposed defect detection system relies on several key parameters, including: The threshold value for segmentation, The structuring element sizes used in morphological processing, The feature set selected for classification. To evaluate the robustness of these parameters, a limited sensitivity analysis was performed on a validation subset of the dataset.
- Threshold value sensitivity.
  Segmentation performance was tested with threshold values ranging from *0.25* to *0.40* in increments of *0.01*. The optimal result, in terms of IoU and F1-score, was consistently achieved at *0.32*, confirming its suitability for the dataset. Higher thresholds resulted in under-segmentation (missed defects), while lower thresholds increased false positives due to noise.
- Structuring element sensitivity.
  Two sets of rectangular structuring elements were used for morphological operations: $[4\times3]$ and $[8\times6]$. Experiments with alternative sizes $(\text{e.g., } [3\times2],\ [5\times5],\ [10\times8])$ showed either loss of small defect regions or over-smoothing of features. The selected sizes provided the best balance between noise reduction and preservation of defect edges.
- Classifier input features
  All 12 extracted features were included in the PCA input. To test classifier robustness, models were retrained using a reduced feature set (excluding low-variance components). Results showed a *5-7%* drop in classification accuracy, confirming that the full feature set contributes meaningfully to defect discrimination.

4. Conclusion

The complicated issues of noise, low contrast, and uneven illumination of scanned radiography images can be resolved by the suggested procedures, leading to positive outcomes. The proposed research work leads to the following conclusions:

- Despite being excessively expensive, the traditional digital radiography technology is widely utilized for automated flaw identification and categorization. The technique employed in this study, which is based on scanning casting radiography, is quite inexpensive and has shown itself to be most effective in small-scale applications.
- This research project uses a mix of Gaussian low pass filter and adaptive winner filter, one of the accessible picture pre-processing techniques. For detecting casting defects, this combination performed as effectively suitable for casting defect detection.
- It has been determined that the multi-stage morphological image processing concept is ideal for casting flaw identification. This is a completely novel idea that no previous researchers have ever employed.
- Compared to the ideal threshold value recommended by Ostu's Segmentation Algorithm, the experimental threshold value of *0.32* was determined to be the best suitable for threshold-based picture segmentation. 56 radiography photos with a range of flaws are used to assess this value.
- Using a Multi-Layer Feed-forward Artificial Neural Network, defect classification accuracy ranges from *80%* to *94%*. During testing, a hidden layer with 13 neurones and 5 back-propagation output neurones was determined to be appropriate for classifying defects.
- The novelty lies in the integration and tuning of standard techniques like PCA, Wiener filter, ANN for low-cost, small-scale industrial casting inspection. Additionally, the use of experimentally derived thresholds in morphological filtering and segmentation, optimized specifically for valve castings, is a unique contribution of this work.
- The current processing time per image is about *3* seconds and the method is not yet real-time, it is well-suited for offline inspection.

5. Limitations and future work

5.1. Limitations

While the proposed defect detection system demonstrates promising results, several limitations were observed during experimentation and analysis:

- Limited Dataset Size: The system was developed and tested on 56 radiographic images, which may not fully capture the diversity of casting defects, material types, and imaging conditions encountered in industrial practice.
- Class Imbalance: Certain defect categories, such as "shrinkage" and "tear", were underrepresented in the dataset, leading to relatively lower classification performance for these classes.
- Manual Ground Truth: Segmentation results were validated against expert-annotated ground truth images, but no publicly available dataset was used. This may affect reproducibility and standard benchmarking.
- Over-Segmentation Effects: Although morphological processing enhanced flaw visibility, it occasionally led to over-segmentation due to residual noise, increasing the risk of false positives.
- Non-Real-Time Processing: The current implementation operates in offline mode and requires approximately 3 seconds per image, limiting its applicability in real-time inspection systems without further optimization.
- Black-Box Classification: The ANN model, while accurate, lacks high interpretability. Feature influence is not inherently visible, which may hinder acceptance in safety-critical NDT applications.

5.2. Future Work Directions

To enhance the applicability, scalability, and robustness of the proposed system, the following future research directions are identified:

- Dataset Expansion: Collecting a larger and more diverse set of radiographs representing various casting types, defect geometries, materials (ferrous and non-ferrous), and imaging conditions to improve generalization.
- Class Balancing Techniques: Implementing data augmentation, synthetic oversampling (e.g., SMOTE), and class-weighted training to improve detection of underrepresented defect types.
- Deep Learning Integration: Exploring CNN-based and hybrid deep learning models that can automatically learn spatial features, potentially outperforming handcrafted feature approaches in complex radiographic patterns.
- Model Explainability: Integrating interpretability tools such as SHAP or LIME to analyse feature importance and enhance user trust in AI decisions, especially in regulatory or critical quality control environments.
- Real-Time Optimization: Porting the model to GPU-based platforms or edge devices using model compression techniques (e.g., pruning, quantization) to enable deployment in real-time or in-line inspection workflows.
- Public Dataset Release: Subject to industrial confidentiality clearance, a curated and anonymized subset of radiographs may be shared with the academic community to support benchmarking and collaboration.

Nomenclature

t – threshold
σ_{ω}^2 – weighted sum of variances
σ_1, σ_2 – variances
ω_1, ω_2 – weights

References

[1] Merry D., Filbert D. and Parspour N. (2000): *Improvement in automated aluminum casting inspection by finding correspondence of potential flaws in multiple radioscopic images*.– Int. Proc. 15th World Conf. on Non- Destructive Testing, Rome (Italy), NDT.net, vol.11, https://www.ndt.net/?id=734.

[2] Silva R.R. and da Mery D. (2004): *Accuracy estimation of detection of casting defects in X-ray images using some statistical techniques*.– INSIGHT, J. Br. Inst. Non-Destructive Test, vol.49, No.10, pp.603-609, DOI:10.1007/978-3-540-77129-6_55.

[3] Zapata J., Vilar R. and Ruiz R. (2011): *Performance evaluation of an automatic inspection system of weld defects in radiographic images based on neuro-classifiers*.– Expert Systems with Applications, vol.38, pp.8821-8824, DOI:10.1016/j.eswa.2011.01.092.

[4] Kaftandjian V., Joly A., Odievre T., Courbiere M. and Hantrais C. (1998): *Automatic detection and characterization of aluminum weld defects: comparison between radiography, radioscopy and human interpretation*.– Int. Proc. 7th European conf. on nondestructive testing, NDT.net, vol.3, No.10, pp.1179-1186.

[5] Mery D., Jaeger Th. and Filbert D. (2002): *A review of methods for automated recognition of casting defects*.– INSIGHT, J. Br. Inst. Non-Destructive Test, vol.44, No.7, pp428-436.

[6] Mery D. and Filbert D. (2002): *Automated flaw detection in aluminum castings based on the tracking of potential defects in a radioscopic image sequence*.– IEEE Transactions on Robotics and Automation, vol.18, No.6, pp.890-901, DOI:10.1109/TRA.2002.805646.

[7] Hara Y., Akiyama N. and Karasaki K. (1983): *Automatic inspection system for printed circuit boards*.– IEEE Transactions on Pattern Analysis and Machine Intelligence, vol.5, No.6, pp.623-630, DOI: 10.1109/tpami.1983.4767453.

[8] Nagaswami V.R., Grimeault S. and Dover R.J. (1997): *Application of segmented auto threshold (SAT) for 0.5 mm and 0.35 mm logic interconnects layers*.– IEEE/SEMI Advanced Semiconductor Manufacturing Conference and Workshop.

[9] Maeda S., Kubota H., Makihira H., Ninomiya T., Nakagawa Y. and Taniguchi Y.(1990): *Automated visual inspection for LSI wafer multilayer patterns by cascade pattern matching algorithm*.– Systems and Computers in Japan, vol.21, No.12, pp.65-77, https://doi.org/10.1002/scj.4690211208.

[10] Shapiro A. (1996): *Automatic classification of wafer defects: Status and industry needs*.– Int. Proc. IEEE/CPMT International Electronics Manufacturing Technology (IEMT) Symposium, pp.117-122.

[11] Marino P., Dominguez M.A. and Alonso M.(1999): *Machine-vision based detection for sheet metal industries*.– Int. Proc. IEEE Industrial Electronics Society IECON, San Jose, CA, USA, pp.1330-1335, DOI:10.1109/IECON.1999.819404.

[12] Scaman M.E. and Economikos L. (1995): *Computer vision for automatic inspection of complex metal patterns on multichip modules (MCM-D)*.– IEEE Transactions on Components, Packaging, and Manufacturing Technology, Part B: Advanced Packaging, vol.18, No.4, pp.675-684, DOI: 10.1109/96.482992.

[13] Fernandez C., Fernandez S., Campoy P. and Aracil R.(1994): *Online texture analysis for flat products inspection. Neural nets implementation*.– Int. Proc. IEEE Industrial Electronics Society IECON, vol.2, pp.867-872, DOI: 10.1109/IECON.1994.397901.

[14] Shafeek H.I., Gadelmawla E.S., Abdel-Shafy A.A. and Elewa I.M. (2004): *Automatic inspection of gas pipeline welding defects using an expert vision system*.– NDT and E International, vol.37, No.4, pp.301-307, DOI: 10.1016/j.ndteint.2003.10.004.

[15] Kuang-Chao Fan, Shou-Hang Chen, Jhih-Yuan Chen and Wei-Bor Liao. (2010): *Development of auto defect classification system on porosity powder metallurgy products*.– NDT and E International, vol.43, No.4, pp.451-460, DOI:10.1016/j.ndteint.2010.04.005.

[16] Wu W.Y., Wang M.J.J. and Liu C.M. (1992): *Performance evaluation of some noise reduction methods*.– CVGIP: Graph Models Image Process, vol.54, No.2, pp.134-146, DOI:10.1016/1049-9652(92) 90044-5.

[17] Canny J. (1986): *Computational approach to edge detection*.– IEEE Transactions on Pattern Analysis and Machine Intelligence (PAMI), vol.8, No.6, pp.679-698, DOI: 0162-8828/86/1100-0679$01.00.

[18] Marr D. and Poggio T. (1980): *Theory of edge detection*.– Proceedings of Royal Society, London 1980, vol.B207, pp.187-217, DOI: 10.1098/rspb.1980.0020.

[19] Otsu N. (1979): *A threshold selection method from gray-level histograms*.– IEEE Transactions on Systems, Man and Cybernetics (SMC), vol.9, No.1, pp.62-66, DOI: 0018-9472/79/0100-0062.

[20] Zscherpel U. (2000): *Film digitization systems for DIR: Standards, requirements, archiving and printing*.– NDT.net, vol.5, No.5.

[21] Zscherpel U. (2002): *A new computer based concept for digital radiographic reference images*.– NDT.net, vol.7, No.12.

[22] Haralick R. and Shapiro L. (1992): *Computer and robot vision*.– Addison Wesley, vol.1,pp.28-48.

[23] Mirapeix J., Garcia-Allende P.B., Cobo A., Conde O.M. and Lopez-Higuera J.M. (2007): *Real-time arc-welding defect detection and classification with principal component analysis and artificial neural networks*.– ELSEVIER NDT&E International, vol.40, pp.315-323, DOI: 10.1016/j.ndteint.2006.10.002.

[24] Wagh M., Waghmare C., Gudadhe A., Thakur N., Mohammed S.J., Algburi S., Majdi H.S. and Ansari K. (2025): *Predicting compressive strength of sustainable concrete using advanced AI models: DLNN, RF, and MARS*.– Asian Journal of Civil Engineering, pp.1-16, DOI: 10.1007/s42107-025-01278-y.

[25] Wagh M., George S., Algburi S. Waghmare C., Gupta T., Yadav A. and Majdi A. (2025): *Prediction of ANN, MLR, and NLR models for compressive strength performance in fly ash based self compacting concrete*.– Asian Journal of Civil Engineering, pp.1-14, DOI: 10.1007/s42107-025-01385-w.

[26] Kurzekar A.S., Waghe U., Ansari K., Dabhade A.N., Biswas T., Algburi S. and Palanisamy J. (2024): *Development and optimization of geopolymer-based artificial angular coarse aggregate using cut-blade mechanism*.– Case Studies in Construction Materials, vol.21, e03826, DOI: 10.1016/j.cscm.2024.e03826.

Received: May 11, 2025
Revised: November 21, 2025